NUMERICAL MODELLING OF RAILWAY BALLAST AT THE PARTICLE SCALE

Sharif Ahmed[1] [2], John Harkness[1§], Louis Le Pen[1], William Powrie[1] and Antonis Zervos[1]

[1] *Faculty of Engineering and the Environment, University of Southampton, Southampton, SO17 1BJ, U.K.*

[2] *-VIS X-Ray Imaging Centre, University of Southampton, University Road, Southampton SO17 1BJ, UK*

Keywords: DEM, ballast, particle shape,

SUMMARY

The paper describes the development of a technique to simulate triaxial tests on specimens of railway ballast numerically at the particle scale; and its validation with reference to physical test data. The ballast particles were modelled using potential particles and the well-known discrete element method. The shapes of these elemental particles, the particle size distribution and the number of particles ($N = 2800$) in each numerical triaxial specimen all matched closely the real ballast material being modelled. Confining pressures were applied to the specimen via a dynamic triangulation of the outer particle centroids. A parametric study was carried out to investigate the effects on the simulation of timestep, strain rate, damping, contact stiffness and inter-particle friction. Finally, a set of parameters was selected which provided the best fit to experimental triaxial data, with very close agreement of mobilized friction and volumetric strain behaviour.

1. INTRODUCTION AND BACKGROUND

Ballast is traditionally used to support railway tracks as it is relatively inexpensive and easy to maintain. However, the increasing demands being placed on ballasted track in terms of faster, heavier, tilting and more frequent trains mean that a better understanding of its mechanics, and the way in which it resists lateral and vertical loads, is required.

§ Correspondence to: John Harkness
Email: J.Harkness@soton.ac.uk

It can be difficult to carry out mechanical testing on specimens of railway ballast in traditional laboratory apparatus owing to the large particle size. Thus there is interest and merit in developing simulation techniques that enable the mechanical behaviour of ballast to be investigated numerically at the particle scale. Numerical simulations are also advantageous in enabling the visualisation of structures and force chains, and a more complete understanding of the distribution of local stresses and strains within the specimen as a whole, without reliance on average or boundary measurements as is often the case in laboratory tests. The insights that can be gained from such numerical simulations therefore complement and enhance those from conventional laboratory element testing.

Railway ballast is an ideal subject for discrete element modelling (DEM). The large size of the grains in comparison with the depth of the ballast layer means that, although a continuum approach may still be reasonable, there are relatively few grains to model in a DEM. Furthermore, the inherent heterogeneity of the mechanical behaviour of granular materials like ballast, is best studied at the grain scale, at which the effects of grain shape, roughness and size distribution can be investigated. However, representation of the irregular shape of ballast stones presents a modelling challenge. Spheres are widely used in DEM [1 - 3]; however, there are several different approaches to the modelling of non-spherical particles. Perhaps the most straightforward of these is to attach two or more spheres rigidly together to form each particle [e.g., 4 and 5]. The drawback of this method is that more angular shapes are not efficiently modelled by overlapping spheres so that large numbers of spheres may be needed to model each particle accurately. While real shapes are too computationally intensive for meaningful simulations, several options are available for simplified angular particles to be implemented into DEM [e.g. 6]. This paper uses the potential particle method [7,8], which is efficient for modelling slightly rounded polyhedral particles of moderate complexity.

The question remains, given the ability to model simplified irregular shapes, how much of the real geometry of particles must be captured for an assembly of such particles to model realistic behaviour.

This paper:

- Describes the development of a library of particles that can be used to simulate a crushed rock railway ballast.
- Describes the simulation of a triaxial test, including sample preparation and the application of a confining pressure.
- Presents an investigation into the effects of variations in physical and modelling parameters on the test results and identifies values that match the laboratory behaviour.
- Presents insights into the structure of ballast gained from a DEM simulation of a triaxial test that matches volumetric and strength behaviour to that observed in a physical test.

2. DEVELOPMENT OF NUMERICAL SPECIMEN

2.1. Potential particles

Potential particle shapes take the form of adjustably-rounded convex polyhedra. A numerical solver is used to determine the overlap between any two shapes. For there to be just a single overlap, it is necessary that the shapes are strictly convex, but the degree of roundness can be very small. Mathematically, the shapes are expressed as the level set of a function of a position vector, x, (in other words, the particle surface is formed from the set of points for which the function $f(x)$ has a given constant value). The function can include planes, which correspond to the polyhedral flats, and (optionally) an ellipsoid or sphere, which can be used as the basis of the particle shape. Strict convexity is guaranteed through the addition of a positive spherical or ellipsoidal component to the function value. The potential function $f(x)$ is designed to be a smooth function that obeys

$$f(x)\ is \begin{cases} < 0, x \text{ inside the particle} \\ = 0, x \text{ on the surface of the particle} \\ > 0, x \text{ outside the particle} \end{cases} \quad (1)$$

The surface defined by $f(x) = constant$ must be strictly convex. Given two such particles p_1 and p_2, defined by $f_1(x)$ and $f_2(x)$, it can be established whether p_2 overlaps p_1 by finding the point on the surface of p_1 at which the gradients of the two functions are parallel, denoted by A in Figure 1. This is equivalent to minimizing the function,

$$f_1(x) + \Lambda f_2(x) \quad (2)$$

subject to $f_1(x) = 0$, where Λ is a Lagrange multiplier, a scalar. It follows that:

$$\nabla f_1(x) = -\Lambda \nabla f_2(x) \quad (3)$$

The Lagrange multiplier, Λ, required to allow for different magnitudes in the two gradient vectors, may be eliminated from the set of simultaneous equations given by Equation (3) together with the requirement that $f_1(x) = 0$. A non-linear solver, such as Newton–Raphson, may be used to solve for x. Then, if $f_2(x) < 0$, the two particles are overlapping.

The form of the function used for the potential particles is:

$$
\begin{aligned}
f(x,y,z) \;=\; & (1-k)\left\{\left\langle r_c\left(\sqrt{\frac{x^2}{{r_x}^2}+\frac{y^2}{{r_y}^2}+\frac{z^2}{{r_z}^2}}-1\right)\right\rangle^3 - s^3\right\} && \text{ellipsoidal term} \\
& + (1-k)\sum_{i=1}^{n}\left\langle\frac{a_i x+b_i y+c_i z+d_i}{\sqrt{a_i^2+b_i^2+c_i^2}}\right\rangle^3 && n \text{ added flats} \\
& + kr_c^3\left\{\left(\frac{x^2}{{r_x}^2}+\frac{y^2}{{r_y}^2}+\frac{z^2}{{r_z}^2}\right)^{3/2}-1\right\} && \text{added convexity}
\end{aligned}
\tag{4}
$$

where:

$$
\begin{aligned}
r_x &= k_r r_x^{desired} \\
r_y &= k_r r_y^{desired} \\
r_z &= k_r r_z^{desired} \\
r_c &= max(r_x, r_y, r_z)
\end{aligned}
\tag{5}
$$

and where k_r is a user-specified factor $(0 < k_r < 1)$ that relates the desired radii to the scaled radii ($r_x, r_y,$ and r_z) used in the function. Finally, s and k are positive constants; s affects the roundness of the particle corners and k determines the convexity of any flat surfaces.

2.2. DEM simulation cycle

Discrete (or distinct) element modelling (DEM), as proposed by Cundall and Strack [1], is the dynamic simulation of the mechanical interaction of inertial particles with surface stiffness and frictional properties. In general, DEM code can be split into four main functional areas or modules:

1. Broad phase contact detection. This attempts to optimize the problem of detecting contacting particles without examining every possible pair of particles in a system. The module determines whether object bounding boxes are overlapping. A subsequent test is carried out to determine the true extent of overlap.
2. Contact overlap calculation. For spheres, this step is straightforward. For potential particles, an iterative process is used.
3. Contact model. Having determined the overlap, the contact model is used (together with the relative velocities of the two particles and the material properties) to calculate the inter-particle force,

based on a Hertzian contact model [9, 10]. The component of the force normal to the contact plane is calculated directly as a function of the overlap. The tangential component of force (shear force) is calculated incrementally at each cycle, as follows:

   a. The stored shear force vector is rotated in accordance with rotation (during the previous cycle) of the contact normal and the average particle rotation about this normal.
   b. The relative particle movement for the current cycle is calculated from the relative velocities at the contact point and the current timestep. The product of this movement with the shear stiffness yields a trial value of shear force.
   c. The magnitude of this shear force is limited to the frictional limit set by the product of the normal force and the coefficient of friction.

4. Numerical integration of the equations of motion. The resultant forces and moments on each particle give rise to particle accelerations, which are integrated to determine the updated particle positions and velocities at the next time step. An explicit integration scheme is used in this code.

The evolution of particle positions takes place over a large number of cycles in which new (or obsolete) contacts are created (or deleted), contact forces updated and the new particle positions and velocities calculated for the current timestep. The process is then repeated, as illustrated in Figure 2. The value of the timestep is generally very small for explicit solvers, and is related to the speed of sound in the material through its stiffness and mass density. A more detailed description of the simulation process is presented in [7].

2.3. DEM particle generation

A library of numerical particles was required for the DEM simulation, with sizes and shapes representative of real ballast. The first step in this process was to gather the required ballast shape information, in terms of form and roundness, together with the particle size distribution. The numerical particle shapes were then created to provide a statistical match to this data.

2.3.1. Physical characterization of material shape

In this study two roughly independent measures of particle shape, form and roundness as defined in Barrett [11], were used to characterize the particle shapes.

Form is the largest scale measure and is commonly quantified by considering aspect ratios of the major dimensions of the particles in orthogonal planes [12]. Roundness, or inverse angularity can be measured by quantifying variations in the particle surface with respect to an idealised shape. Surface roughness may be considered a geometric property; however it is arguably also a material property and both its geometric and material effects can be represented by an inter-particle friction coefficient. A more detailed discussion of shape can be found in Blott and Pye [13], while Le Pen et al. [14] discuss methods for measuring form and roundness of ballast particles including the relative merits of two and three-dimensional approaches.

The railway ballast used in this study was sourced from the Cliffe Hill quarry in Leicestershire operated by Midland Quarry Products. This ballast is of the granodiorite type in the igneous group and was crushed to comply with BS EN 13450:2002 grading category A [15]. Shape characterization of this material was carried out as follows. One hundred ballast particles were individually photographed using three orthogonally orientated, digital cameras (Figure 3). The longest (L), intermediate (I) and shortest (S) dimensions of the particles were determined from these images by fitting ellipses using a geometric least squares algorithm [16]. Form can then be quantified using three ratios:

$$\begin{aligned} \text{Elongation} &= I/L \\ \text{Flatness} &= S/I \\ \text{Equancy} &= S/L \end{aligned} \tag{6}$$

Roundness was measured using a modified version of the Ellipseness, as suggested by Le Pen et al. [14] defined as:

$$Ellipseness = \frac{\text{Perimeter of geometric fit ellipse}}{\text{Perimeter of particle}} \tag{7}$$

DEM ballast construction

The DEM ballast particles were created using interactive graphical software developed in house. Starting from a sphere, planes were introduced to create 'flat-spots' on the surface of the sphere. The orientation and location of

these planes can be manipulated with the computer mouse until the desired shape has been obtained. An example of this process is shown in Figure 4. A library of particles was constructed using this method. Some DEM particles are shown alongside their real ballast counterparts in Figure 5. The Form characteristics are compared quantitatively in the modified Zingg plot in Figure 6, and show a reasonably good match between the numerical particle forms and the real ballast. Figure 7(a) shows a visual key to the elongation and flatness measures used in the Zingg plot. Finally, the ellipseness of the real and DEM ballast is compared in Figure 7(b). The slightly higher values of ellipseness for the DEM particles are as a result of the smooth edges between the major corners as compared to real ballast (where the surface undulates between the major corners). Matching the minor surface undulations for DEM particles would be computationally prohibitive and, as this paper demonstrates, not really necessary.

2.4. Modelling the membrane

Instead of modelling an elastic membrane directly, the essential function of the membrane (to apply a confining pressure to the exterior of the specimen) was simulated by constructing a triangular mesh joining the centroids of particles on the surface of the specimen. The confining force on each triangle was calculated as the product of the confining pressure and the area of the triangle. This force was then distributed to the particles in proportion to the relative cross-sectional areas of the spheres circumscribing them.

Consideration must be given to the interface between the specimen and the edge of the platen. In a real triaxial cell, the edges of the cylindrical membrane extend onto the sides of the platens and are usually held in place with O rings, but also by friction once the confining pressure has been applied. This platen/membrane interface is represented by introducing two circular rings of nodes, fixed to the top and bottom platens, which become part of the mesh. The radii of these rings are set equal to the average effective radii of the specimen adjacent to the top and bottom platens respectively.

2.4.1. Surface mesh construction

If the centroids of the particles in a specimen are considered as a cloud of points, an outer surface can be defined consisting of a triangular mesh (with nodes at the centroids of the particles) which wraps around the outside

of the cloud. One method of identifying a surface mesh is to examine the network formed by the contacts between particles and then determine a contiguous mesh of triangles on the outer surface of the point cloud (see for example [3]). In this case, a different approach was adopted, which makes use of the computational geometry library CGAL [17]. First, a Delaunay triangulation was carried out over all the particle centroids. The surface mesh was then found as a subset of the Delaunay triangulation, an 'alpha shape' as described below.

For a set $\boldsymbol{P}$ of points in 3-dimensional Euclidean space, the Delaunay triangulation is a triangulation $DT(\boldsymbol{P})$ such that no point in $\boldsymbol{P}$ is inside the circumscribing sphere S_i of any tetrahedron in $DT(\boldsymbol{P})$. In 3 dimensions, the triangulation refers to the subdivision of the space into tetrahedra, whose vertices are the points $\boldsymbol{P}$. For a 3-dimensional point cloud the outer surface of this Delaunay triangulation will be a mesh of triangles formed from the tetrahedral faces that have no adjacent tetrahedron. This triangle mesh will always form a convex polyhedron that encloses the point cloud as if a thin elastic sheet were stretched over the cloud of points. For the purpose of transferring a confining pressure to the outer particles, this mesh is not useable as it does not (generally) hug the shape of the cloud.

In two dimensions, no point can be inside the circumscribing circle of any triangle. Figure 8(a) shows the Delaunay triangulation of a small cloud of points in $\mathbb{R}^2$. It can be seen that the perimeter of the triangulation does not include the points A and B. In the context of a virtual membrane, this would mean that the particles corresponding to points A and B would not be subjected to a confining force. To include A and B in the perimeter, it is necessary to remove some of the outer Delaunay triangles – in this case, triangles A and B in Figure 8(b). The mechanism for achieving this is to limit the maximum radius of the circle circumscribing a triangle. For the outer triangles of a triangulation, the circumscribing circles can be very large as there are no points to interfere, as illustrated by the circumscribing circles for triangles A and B. By limiting the maximum permissible circle radius, these surface triangles can be removed from the triangulation, leaving a surface which conforms more closely to the shape of the point cloud as shown in Figure 8(c).

The extension of this principle to 3 dimensions involves limiting the maximum radius of the circumscribing sphere of a tetrahedron, S_i. This is included in the CGAL library via the parameter $\alpha = (maximum\ sphere\ radius)^2$. The effect of varying alpha on the triangulation of a triaxial specimen can be seen in Figure 9. As the shape of a point cloud is somewhat vague, obtaining a suitable fit requires some human input in the selection of α. If α is too large, some of the surface particles will be missed out. On the other hand if α is too small, the triangulation can penetrate into the body of the point cloud (or even form isolated internal pockets). This would lead to undesirable behaviour, but in practice it is relatively easy to choose a suitable (and safe) value for α. The method for tuning α, which was done only once and the resulting value used in all of the subsequent simulations, is to start with a large value and reduce it until all of the clearly visible surface particles are included in the membrane. The chosen value was $\alpha = (maximum\ particle\ radius * 1.5)^2$. Because the model consisted of a relatively dense assembly of particles, the problem of virtual membrane penetration did not occur.

2.4.2. Volume measurement

Two approaches were used to calculate the void ratio; a computationally fast method involving a small approximation, performed during the simulation, and a very accurate but slower method that could be used during post-processing for selected states. For very accurate measurements, a three-dimensional scan of a region within the specimen was made. The region was subdivided into a rectangular array of voxels and each point tested for inclusion within a particle. The void ratio could then be determined from these data. The fast method involved calculating the volume of the polyhedron formed by the virtual membrane and platens, calculated as the sum of the signed (positive or negative) volumes of tetrahedra formed from a common reference point and each triangle of the polyhedron. The solid volume contained within this polyhedron was approximated as the sum of the volumes of the internal particles plus *half* (wherein lies the approximation) of the volume of the surface particles. The volumetric strain shown in the graphs in this paper were calculated using this method.

2.4.3. General remarks on modelling the triaxial cell

A real triaxial cell is not a perfect instrument and must operate within the limitations set by real materials and equipment. One such limitation is the latex membrane,

placed around the specimen, which serves as a boundary between the specimen and the confining fluid. Confining pressure is applied via the membrane and changes in the volume enclosed by the membrane are used to determine volumetric strain. The use of a latex membrane is a practical engineering solution to this problem, but is less than ideal. A particular problem with specimens comprising large particles is that, as the confining pressure is increased, the membrane distorts inwards into the voids between the particles (membrane penetration). This introduces a potentially significant error into the determination of void ratio and volumetric strain. A further undesirable effect is that, as the membrane is stretched and the specimen distorts, it is likely to impose local shear forces on the surface of the specimen together with an additional hoop stress.

A numerical model is not subject to these physical limitations and a balance needs to be struck between producing an accurate model of a real triaxial cell and a model of an idealized triaxial cell. While it is necessary to produce a model that is reasonably faithful to the real cell, as comparison with the results from real tests is essential for the validation of the numerical model, it would be undesirable to expend excessive effort in simulating the shortcomings of the real system. In general this latter approach to modelling - i.e. an idealised triaxial cell - has been adopted. No attempt was made to model the true behaviour of a latex sheet, concentrating instead on the function of a membrane; the application of confining pressure and the measurement of specimen volume. It is therefore necessary to maintain an awareness of the difference between the real and numerical models when comparing the results.

3. NUMERICAL TRIAXIAL TESTS

3.1 Overview of materials modelled and modelling parameters studied

Numerical ballast was generated using the validated library of particle shapes, scaled to match the particle size distribution of the real material. The preparation of a numerical specimen for triaxial testing is described in section 3.2. For a given specimen, there are five principal numerically variable modelling parameters that can influence the results:

1. Time step
2. Shearing speed
3. Damping
4. Contact stiffness
5. Inter-particle friction

Time step and shearing speed are considered as purely numerical parameters whose value needs to be selected to have no significant influence on results. The contact stiffness and inter-particle friction have a physical significance. Their values need to be calibrated to match physical test data for the behaviour of the whole triaxial sample. Although these parameters could perhaps be measured directly (e.g. [18]), there are significant difficulties in achieving this and no values for ballast are available in the literature. Damping is often used in DEM modelling to represent some of the energy losses present in a physical system, but also to remove spurious energy that may be introduced as a result of inaccuracies in the time integration method. A common form of numerical damping, which is used in this study, is the somewhat artificial non-viscous damping proposed by Cundall [19]. The effects on the response of different damping values are explored. Selection/calibration of these five parameters was considered in turn through a series of numerical simulations (Table 1). Results for each simulation were generated as graphs of mobilized angle of shearing resistance and volumetric strain against axial strain as a means to evaluate the influence of varying the parameter. Interpretation of the shearing speed was additionally based on a consideration of a measure of inertia.

A more detailed discussion of the numerical and physical significance of each of these parameters is given in subsections 4.3.1 to 4.3.5.

Results from real triaxial tests on a specimen of 1/3 scale, parallel graded ballast were used for comparison and to calibrate some of the numerical parameters studied. This material can reasonably be tested in a standard 150 mm diameter × 300 mm height triaxial specimen since the largest particle will be less than 1/6 of the specimen diameter [20].

A detailed study of ballast particle shapes [14] demonstrated that the differences in shape (form, roundness) between the physical 1/3 scale and full size ballast were relatively minor. The DEM shapes used fell within the range of real particle forms for both the scaled and full size ballast. Also, a comparison of triaxial test results for scaled ballast (tests reported in this paper) and full size material (reported in the literature) confirmed that mobilized peak angles of shearing resistance for the scaled ballast were within the range of results reported for full size ballast [21].

Particle fracture strength is also sometimes modelled in DEM. A potential difficulty with scaled tests is that fracture strength is known not to scale with particle size, with smaller particles being statistically more fracture resistant [22]. Sieving of the scaled ballast after the physical tests did not show any measurable breakage at the relatively low confining pressures used (< 200 kPa), but breakage could become more significant with increasing particle size and confining stress.

The numerical triaxial test specimens were given particle and sample dimensions equivalent to the physical tests on 1/3 scaled ballast. However as the numerical tests were implemented without gravity these dimensions are only significant in relative terms and the numerical results could equally apply to specimens of full size ballast 450 mm in diameter.

3.2. Triaxial test specimen preparation

The procedure used to prepare a DEM specimen is analogous to the preparation of a triaxial test specimen in the laboratory. At the start of the process, the differently shaped DEM ballast particles are combined and scaled to

obtain a given mass of particles with a desired particle size distribution (PSD). The PSD is given, in terms of sieve sizes and retained masses, in Table 2. A smooth distribution of DEM particle sizes was obtained by interpolation of these data. Each specimen consist of 2800 particles where the D50 is 13.5 mm.

Bagi [23] and Jiang [24] provide concise reviews of the several methods that can be used to create the initial arrangement of particles in a DEM specimen. The dynamic method was adopted in this work. The particles were randomly positioned within a domain space described by a cylinder 1 m high and 0.15 m in diameter, with a very loose initial packing. For reasons of computational efficiency, the particles were initially represented by spheres circumscribing the potential particle shapes (Figure 10a). The particle material stiffness of the particles was set to the value used during the shear test simulation and the inter-particle friction angle ϕ_μ was set to zero.

The model was cycled with high damping to remove any large overlaps between particles. Once the system had settled, the spheres were replaced by the potential particles as shown in Figure 10b. At this point, the frictionless particles were allowed to fall under the influence of gravity, together with the top platen which was assigned a mass of 1 kg. The initial volume of particles was calculated such that the desired void ratio was obtained when the cylinder reached a height of 0.3 m. The system state was saved at regular intervals during this settling phase and when the cylinder height was approaching the desired height, the inter-particle friction angle and damping were set to their final values and the model cycled to equilibrium. The desired void ratio was achieved by a process of trial and error. A typical finished specimen is shown in Figure 11(a).

The virtual membrane was then created around the particles as shown in Figure 11(b). Virtual particles, which do not interact with the ballast particles, were created for the purpose of the triangulation over the platens (Figure 11c). The specimen was then isotropically compressed to the desired confining pressure. The top and bottom platens were represented by horizontal planes, with friction angle and stiffness equal to that of the particles in the specimen.

3.3. Monotonic test results

3.3.1 Effect of time step

For stability of the explicit time integration method used to update the particle positions, the time step must not exceed a critical value t_{crit}. The critical timestep is calculated by considering each particle and the system of contacts around it. This sub-system has a mass (of the particle) and a stiffness provided by the contacts with the surrounding particles, and an approximate natural frequency can be calculated for the translational and rotational movements associated with each axis. The critical timestep is then related to this natural frequency such that

$$t_{crit} = \begin{cases} \sqrt{m/k^{tran}} & \text{(translational motion)} \\ \sqrt{I/k^{rot}} & \text{(rotational motion)} \end{cases} \quad (8)$$

Where k^{tran} and k^{rot} are the translational and rotational stiffnesses, I is the moment of inertia and m is the mass [25]. This calculation is carried out for all the particles in the system and the smallest critical value is taken as the timestep for the whole.

Owing to the approximate nature of the mechanically determined critical timestep, it is common practice to use a fraction of the calculated critical timestep as the actual time increment such that

$$\Delta t = \alpha_{sf} t_{crit} \quad (9)$$

where α_{sf} is termed the safety factor. Itasca [25] recommend α_{sf}=0.80 for simulations using the linear contact law and 0.25 for simulations using a Hertz-Mindlin contact law.

While the use of a safety factor helps to improve the robustness and accuracy of the automatic timestep determination, it will increase simulation time and cost. For $\alpha_{sf} = 0.25$, the simulation time will in theory take four times as long to run as with the critical timestep, $\alpha_{sf} = 1.0$. It is therefore important to choose a value for α_{sf} that balances simulation accuracy and computational cost. To determine the effects of timestep size, four simulations were carried out using safety factors (α_{sf}) of 0.20, 0.50,

0.95 and 1.00 (Table 3). $\alpha_{sf} = 1.0$ was used as the benchmark value. The specimen was prepared using the method already described and only the value of α_{sf} was varied between simulations.

Figure 12 shows the mobilized strength and volumetric strain plotted against axial strain for this series of simulations. The initial responses of the three simulations are nearly identical. The maximum compressive volumetric strain, reached at approximately 4% axial strain, is very similar for all simulations. Beyond this point, all simulations dilate monotonically with TS1 and TS2 having similar rates of dilation (approximately 0.17), but TS3 and TS4 appear to exhibit a slightly lower rates of dilation of approximately 0.12. The peak effective friction angle, the effective friction angle at the end of the simulation and the maximum volumetric strain are summarised in Table 3. There are generally only small variations between the simulations, with TS1 and TS2 being very closely matched.

The data in Figure 12 and Table 3 show that the timestep affects the results of a DEM simulation. Larger timesteps result in higher kinetic energies, causing vibration of the specimen and leading to a small suppression of dilation due to dynamic rearrangement. The mechanically determined critical timestep may be used as an initial estimate, and in this case a safety factor $\alpha_{sf} = 0.5$ provides a balance between stability and computational cost.

3.3.2. Effect of shearing speed

The shearing speed of a laboratory triaxial cell experiment on a non-clay soil is typically between 0.5 and 0.001 mm/minute (0.0023 to 0.000006% of the specimen height per second) [26]. To match this rate in the simulation would take too long (months), owing to the small timestep and the computational work required at each step. Thus faster shear speeds were used in the simulations to reduce the run time to an acceptable level. If the rate of deformation were too fast, the model response would be dynamic representing rapid granular flow rather than the quasi-static behaviour seen in a triaxial test. The chosen shear velocity must therefore be slow enough to induce a quasi-static soil response yet fast enough to give realistic run times. Triaxial shear test simulations were carried out at three strain rates (Table 4).

The nature of the response (plastic/static or visco-plastic/dynamic) can be determined with reference to the inertia number I_n,

$$I_n = \dot{\varepsilon}_q \sqrt{\frac{m}{pd}} \tag{10}$$

where $\dot{\varepsilon}_q$ is the shear strain rate (0.2, 0.02 and 0.02 m/s), m is the mass of the particle (0.0888 kg), p is the confining cell pressure (15 kPa) and d is the particle diameter (0.0135 m) [3,27,28]. Previous authors have shown that small inertia numbers are associated with a network of enduring contacts in quasi-static conditions [29], while larger inertia numbers correspond to the dynamic inertial regimes seen in rapid flow or binary collision [30]. It is generally recommended that $I_n \ll 1$ to ensure quasi-static plastic behaviour.

The maximum inertia numbers for the simulations V4, V5 and V6 were 4.19×10^{-3}, 4.19×10^{-4} and 4.19×10^{-5}, respectively Given a limiting inertia number of 10^{-2} [27], the response in all three simulations should be quasi-static.

Figure 13 shows the mobilized friction angle and volumetric strain against axial strain for simulations V4 – V6. The effect of strain rate on peak effective friction angle is

minimal. The peak effective friction angle in V4, (133%/s) is 2.77° higher than that in V5, while in V6 ϕ'_{peak} varies by 0.66° (Table 4).

3.3.3. Effect of Damping

When real granular material is strained, kinetic energy is dissipated at the contacts through a combination of microscopic processes such as friction and yielding of surface asperities. The contact model used in the DEM simulations reported in this paper was elastic for movement parallel to the contact normal and elastic/perfectly plastic for relative tangential movement. Under certain conditions, this idealized model can result in less energy dissipation than in a real system. Thus damping is commonly used to control any non-physical vibration that may arise as a result of excess kinetic energy in the model.

The damping formulation used in the simulations reported in this paper was based on the local damping proposed by Cundall [19], in which 'the damping force is proportional to the magnitude of the out-of-balance-force at each node, acting so as to damp rather than encourage vibration'. The damping force is given by

$$F_d^i = -\alpha_d \left|\boldsymbol{F}_o^i\right| sign(V^i) \qquad (11)$$

where α_d is the damping constant, $\left|\boldsymbol{F}_o^i\right|$ is the magnitude of the out-of-balance force for the ith degree of freedom ($i = 0,1,2$), V^i is the velocity of the particle and $sign()$ indicates the sign (positive or negative) of the particle velocity [25,31].

Three values of damping coefficient (α_d = 0.05, 0.1 and 0.7) were investigated in addition to a simulation in which damping was switched off (i.e. α_d = 0), as summarized in Table 5. An equivalent value of the fraction of critical damping ratio, ζ, is also given, based on the approximation $\zeta \cong {}^{\alpha_d}/_{\pi}$, valid for low values of damping [25]. The same initial specimen was used in all four tests. After the desired confining (cell) pressure had been applied, the damping constant was changed and the model was cycled to equilibrium, bringing the specimen into a steady state under the new damping conditions.

Figure 14 shows the mobilized strength and volumetric strain as a function of shear strain for simulations D7-D10. Increasing the damping increases both the peak effective friction angle and the rate of dilation (Table 5). Similar findings were also reported by Ng [32]. A damping constant of 0.7 is clearly too high and has a dramatic impact on the model response. On the other hand, zero damping is perhaps unrealistic as there is no mechanism for energy dissipation if contacts are operating elastically (below the plastic limit). For this reason, a small value of damping ($\alpha_d = 0.05$) was chosen for the calibration runs in section 4.1.2, although zero damping could also have been used with very little effect on the results.

3.3.4. Effect of contact stiffness

For Hertzian contacts, the inter-particle stiffness *K* is a function of the particle material shear modulus, G, and the effective radius of curvature local to the contact. For rough surfaces, this radius of curvature may be much smaller than the idealized, smooth, particle shapes and there is therefore some uncertainty in the choice of the stiffness value. To assess the influence of shear modulus on the response of the model, simulations were carried out with G=1 GPa and G=10 GPa.

The contact stiffness at which a specimen is brought to equilibrium can affect the configuration of the particle matrix. To minimize any variation in fabric between the two specimens, the contact stiffness of CS11 was changed and cycled to equilibrium with all boundary motion inhibited (e.g. [32 and 33]). A small change in the void ratio was apparent (see Table 6) along with minor movements in the particle matrix. The average displacement of particles was 0.0002% of the average particle diameter.

Figure 15 shows that changes in the contact stiffness have an effect on the rate at which strength is mobilized with shear strain. While the peak strengths are similar (with a difference of less than 1°), the initial responses are distinctly different. This can be explained by the volumetric strain behaviour of the two tests seen in Figure 15. Increasing the contact stiffness reduces the bulk elastic deformation, resulting in the stiffer initial response of mobilized effective friction angle against shear strain. The simulation run time is also affected by

the contact stiffness, with the higher stiffness found to increase simulation run time by at least 100%.

3.3.5. Effect of inter-particle friction angle

Three different values of inter-particle friction angle ϕ_μ were used to assess the effect on the mechanical response of the model (Table 7). The settled specimen for IF15 was used as the initial specimen for the other tests. The inter-particle friction angle was reduced to the required value and the model was allowed to come to equilibrium, to avoid pre-stressing.

While there was no change in the initial void ratio, specimens prepared in this way will be prone to changes in contact state and force chain configuration during shear. Contacts that were initially stable (at the higher ϕ_μ) will inevitably become closer to sliding as ϕ_μ is decreased. However, even by the end of the shear test simulation with the largest change (i.e. IF15), only 0.003% of contacts had changed state.

Figure 16 shows the behaviour expected of a granular material as the inter-particle friction angle is increased, with generally higher peak strengths being mobilized at a lower axial strain. The initial rate of compression is reduced, dilation starts at a smaller strain and the rate of dilation is increased. The number of sliding contacts reduces with increasing inter-particle friction angle, with IF15 (ϕ_μ = 40°) having 63% fewer at 16% axial strain, and IF 14 (ϕ_μ = 35°) having 38% fewer than IF13 (ϕ_μ = 30°). Reducing ϕ_μ promotes an apparently less stiff and less dilatant response and could be used as a proxy for particle abrasion and breakage, which is argued by McDowell and Bono [34] to be responsible for the reduction in peak strength, stiffness and dilation of soils with increasing confining (cell) pressure.

4. COMPARISON WITH PHYSICAL TEST DATA

4.1. Model calibration

It is generally accepted that DEM models are able to replicate the basic characteristics (e.g. dilatancy, shear localization, stress dependence,) of the stress-strain behaviour of granular media. The input parameters that govern this behaviour can be broadly classified into geometrical properties (particle shape and size distribution) and mechanical properties (type of contact model, contact stiffness and inter-particle friction).

Recent advances in modelling particle geometry have meant that researchers are no longer restricted to using simple spheres (or clumps of spheres). As already discussed, concepts such as potential particles [7], can be used to create DEM particles which are characteristic of real materials. Similarly, the implementation of realistic PSD's in simulations is commonplace.

However, this not the case when considering the mechanical properties. It is possible in principle, but in practice difficult, to measure the contact stiffness and inter-particle friction angle; and there are few data on these properties for real materials. Furthermore, the simplification of the complex contact mechanics of a real granular system in a discrete element model means there is no guarantee of accurately capturing the response, even if measured parameter values are used. It is therefore usually necessary to calibrate a DEM model with reference to data obtained in a real laboratory test.

4.1.1. Calibration method

The calibration process was carried out to match, as closely as practically possible, the macroscopic behaviour of the DEM model to that of laboratory triaxial cell experiments with similar boundary conditions. The calibrated parameters were the inter-particle contact stiffness K and the inter-particle friction angle ϕ_μ.

The method used was a simple two-step process, similar to that described by [35]. First, adjustments were made to the inter-particle friction angle until the volumetric strain behaviour of the real material was captured. At the same time, the peak effective friction angle (angle of shearing resistance) ϕ'_{peak} was monitored as a means of measuring the suitability of the adjustment. Secondly, the contact

stiffness K was varied until the deformation characteristics seen in the laboratory results were reproduced.

The benchmark laboratory triaxial test was carried out by Aingaran [36] on 1/3 scale ballast (BS EN 13450:2002 grading category A reduced by a factor of 1/3) from Cliffe Hill quarry, Nottinghamshire, UK, sheared monotonically under an effective confining (cell) pressure of 15 kPa. The initial specimen dimensions were 300 mm high × 150 mm diameter. CT image analysis showed that unloaded laboratory specimens had a void ratio of 0.65 and approximately 2800 particles [37]. The specimen for the DEM simulation was prepared as already described, with the specimen dimensions, particle size distribution, number of particles and initial void ratio matched as closely as possible to those of the real specimen.

4.1.2. Calibrated model parameters.

The parameter values obtained by calibration are summarized in Table 8. The results of triaxial test simulations carried out using these parameters are compared with laboratory test data from two tests at 15 kPa confining pressure in Figure 17. Agreement is very close, with the calibrated model capturing both the strength and dilatancy characteristics of the real material. There is a small variation in the laboratory data and the simulation lies, on the whole, in the same range.

5. CONCLUSIONS

A new method has been proposed for simulating the behaviour of railway ballast in monotonic triaxial tests, using the innovative 3D potential particle approach and the well-known discrete element method. The elemental particles, PSD and number of particles in each numerical specimen all matched closely the ballast material being modelled.

A parametric study was carried out to investigate the effect on the results of the simulation of five parameters: timestep, shearing velocity (or strain rate), damping, contact stiffness and inter-particle friction. The first three of these are devices associated with the numerical modelling approach, and the criterion for selecting a particular value is that the value chosen should neither influence the results of the simulations unduly nor make the simulation inefficient or overly expensive in terms of time or computational power.

The choice of simulation timestep is a trade-off between accuracy on one hand and simulation run time and stability on the other. The parametric studies indicated that reducing the timestep below half of the theoretical value did not significantly affect the response. For larger timesteps, up to the critical value, a small reduction in dilation rate was observed. Therefore for accuracy, a safety factor of 0.5 is recommended.

Time constraints will almost always preclude the use of real-time strain rates in DEM triaxial test simulations, and those presented in this paper were no exception to this. It was found that the strain rate did not adversely affect the overall response as long as it was less than 13.3% per second.

The results showed that damping should ideally be kept as low as possible as it not only affects the response of the material but also adversely influences the duration of the simulation. A range in the damping coefficient from zero to 0.1 was shown to have minimal effect in both respects.

The contact stiffness and the inter-particle friction angle are both in theory measurable, but obtaining realistic and relevant values is practically difficult. The simulations have shown that reducing the inter-particle friction will reduce the peak strength, the initial global specimen stiffness and dilation, suggesting that it could be used as

a proxy for particle abrasion/breakage at higher at higher confining stresses.

Following calibration for the inter-particle friction angle and contact stiffness parameters, the model was able to reproduce satisfactorily the overall response of a scaled ballast in a monotonic triaxial shear test. Very close agreement was achieved in the mobilized strength/shear strain, volumetric strain/shear strain and mobilized strength/rate of dilation behaviour.

ACKNOWLEDGEMENTS

The authors are grateful for the financial support of the Engineering and Physical Sciences Research Council through the grant entitled "Development and role of structure in railway ballast" (Reference: EP/F062591/1) and the Programme grant TRACK21 (EP/H044949/1).

LIST OF SYMBOLS

α_d	damping constant
α_{sf}	timestep safety factor
$\dot{\varepsilon}_q$	is the shear strain rate
ζ	Damping ratio
ϕ_μ	inter-particle friction angle
ϕ'_{peak}	peak effective friction angle
Λ	Lagrange multiplier required to allow for different magnitudes in the two gradient vectors
d	particle diameter
k	positive constants affecting the convexity of any flat surfaces
k_r	a user-specified factor $(0 < k_r < 1)$ which relates the desired radii to the scaled radii ($r_x, r_y,$ and r_z)
k^{rot}	rotational stiffness
k^{tran}	translational stiffness
m	mass
p	confining cell pressure

$r_{x,y\ and\ z}$	scaled radii
t_{crit}	critical timestep
F_d^i	Damping force
G	Shear modulus
I	Intermediate dimension/diameter of a particle
I_n	moment of inertia
$I_{no.}$	inertia number - determines nature of the response (plastic/static or visco-plastic/dynamic)
K	Contact stiffness
L	Longest dimension/diameter of a particle
P	Set of points in 3-dimensional Euclidean space
S	Shortest dimension/diameter of a particle
S	positive constants affecting the roundness of the particle corners
S_i	circumscribing sphere
V^i	Particle velocity

REFERENCES

1	Cundall, P A, Strack, ODL. Discrete numerical model for granular assemblies. *Geotechnique* 1979; **29 :** 47–65.
2	Thornton, C. Numerical simulations of deviatoric shear deformation of granular media. *Geotechnique* **2000; 50(1),** pp. 43–53.
3	O'Sullivan, C. Particulate discrete element modelling: a geomechanics perspective. Oxon: Spon Press. 2011.
4	Powrie, W, Ni, Q, Harkness RM, Zhang, X. Numerical modelling of plane strain tests on sands using a particulate approach. *Géotechnique* 2005; 55(4), pp. 297-306
5	Ferellec, J-F, McDowell, GR (2010). A method to model realistic particle shape and inertia in DEM. *Granular Matter* **2010; 12(5),** pp. 459–467. doi:10.1007/s10035-

	010-0205-8
6	Radjaï, F. Dubois, F. (eds.). Discrete Numerical Modeling of granular materials: Hardcover, Wiley-Iste, ISBN 978-1-84821-260-2, 2011.
7	Harkness, J. Potential particles for the modelling of interlocking media in three dimensions. *International Journal for Numerical Methods in Engineering*, **2009; 80(12)**, pp. 1573–1594. doi:10.1002/nme.2669
8	Houlsby, GT. Potential particles: a method for modelling non-circular particles in DEM. *Computers and Geotechnics*, **2009; 36(6)**, pp.953–959.
9	Hertz, HR. *Miscellaneous Papers*, London, MacMillan and Co. Ltd, New York, Macmillan and Co. 1896
10	Johnson, KL. *Contact mechanics*, Cambridge University Press. 1985
11	Barrett , PJ. The shape of rock particles, a critical review. *Sedimentology*, 1980; **27 :** 291-303.
12	Zingg, T. Contribution to the gravel analysis (Beitrag zur Schotteranalyse). Schweizminer. Petrog. Mitt, 15(38-140). 1935
13	Blott, SJ, Pye, K Particle shape: a review and new methods of characterization and classification. *Sedimentology*, 2008; **55 :** 31-63.
14	Le Pen, L, Powrie, W, Zervos, A, Ahmed, S. and Aingaran, S. Dependence of shape on particle size for a crushed rock railway ballast. *Granular Matter*, **2013; 15(6)**, pp.849-861. doi:10.1007/s10035-013-043
15	MQP. Aggregates. Available at: http://www.mqp.co.uk/aggregate.htm [Accessed January 18, 2013].
16	Gander, W, Golub, GH, Strebel, R. Least-squares fitting of circles and ellipses. *Bit*, **1994; 34(4)**, pp.558–578.
17	Sylvain Pion and Monique Teillaud. 3D triangulations. In CGAL User and Reference Manual. CGAL Editorial Board, 4.5 edition, 2014.
18	Cavarretta, I, Coop, M, O'Sullivan, C. The influence of particle characteristics on the behaviour of coarse grained soils. *Geotechnique* 2010, **60:** 413-423.
19	Cundall, PA. Distinct Element Models of Rock and Soil Structure. In E. T. Brown (Ed.), *Analytical and Computational Methods in Engineering Rock Mechanics,* George Allen & Unwin, London. 1987;129-163.
20	Marachi, ND, Chan, CK, Seed, HB. Evaluation of Properties of Rockfill Materials. *Journal of the Soil Mechanics and Foundations Division, Proceedings of the American Society of Civil Engineers* 1972; **98**, pp.95-114.

21	Le Pen, L, Bhandari, AR, Powrie, W. Sleeper end resistance of ballasted railway tracks. *Journal of Geotechnical and Geoenvironmental Engineering* **2014; 140(5).**
22	Mcdowell, GR. Statistics of soil particle strength. *Geotechnique* **2001; 51(10),** pp.897-900. doi:10.1680/geot.2001.51.10.897
23	Bagi, K. An algorithm to generate random dense arrangements. *Granular Matter* 2005; **7 :** 31–43. doi:10.1007/s10035-004-0187-5
24	Jiang, MJ, Konrad, JM, Leroueil, S. An efficient technique for generating homogeneous specimens for DEM studies. *Computers and Geotechnics*, 2003; **30 :** 579–597. doi:10.1016/S0266-352X(03)00064-8
25	Itasca. PFC3D 4.0 *Particle Flow Code in Three Dimensions, Theory and Implementation Volume*. (3rd ed.). Minneapolis, Minnesota. 2008.
26	Head, KH. *Manual of soil laboratory testing. Volume 3, Effective stress tests*. (2nd ed.). Chichester: Wiley. 1988; p.428.
27	G.D.R Midi. On dense granular flows. *The European Physical Journal E*, 2004; **14(4)**, pp.341–365. doi:10.1140/epje/i2003-10153-0
28	Radjai, F. Force and fabric states in granular media. In S. Luding & M. Nakagawa (Eds.), *Proceedings of the 6th International Conference on Micromechanics of Granular Media* Golden, Colorado, 13-17 July 2009, pp.35–42.
29	Iordanoff, I, Khonsari, MM. Granular Lubrication : Toward an Understanding of the Transition Between Kinetic and Quasi-Fluid. Journal of Tribology 2004; 126(1), pp.137–145. doi:10.1115/1.1633575
30	Roux, J, Combe, G. Quasistatic rheology and the origins of strain. *Comptes Rendus Physique* **2002; 3(2)**, pp.131–140.
31	Potyondy, DO, Cundall, PA. A bonded-particle model for rock. International Journal of Rock Mechanics & Mining Sciences 2004; **41 :** 1329–1364. doi:10.1016/j.ijrmms.2004.09.011
32	Ng, T. Input Parameters of Discrete Element Methods. *Journal of Engineering Mechanics.* July 2006 : 723–729.
33	Calvetti, F. Discrete modelling of granular materials and geotechnical problems. *European Journal of Environmental and Civil Engineering* **2008; 12(7-8),** pp.951–965. doi:10.3166/EJECE.12.951-965
34	McDowell, GR, de Bono, JP. On the micro mechanics of one-dimensional normal compression. Géotechnique, **2013; 63(11)**, pp.895-908.

35	Belheine, N, Plassiard, JP, Donzé, FV, Darve, F, Seridi, A. Numerical simulation of drained triaxial test using 3D discrete element modeling. *Computers and Geotechnics* **2008; 36(1-2)**, pp.320—331. doi:DOI: 10.1016/j.compgeo.2008.02.003
36	Aingaran, S. Experimental investigation of static and cyclic behaviour of scaled railway ballast and the effect of stress reversal. *Ph.D. dissertation*, Faculty of Engineering and the Environment, Univ. of Southampton, Southampton, U.K. 2014.
37	Le Pen, L, Ahmed, S, Zervos, A, Harkness, J, & Powrie, W. Resin Recovery and the use of Computed Tomography for Quantitative Image Analysis of Railway Ballast. *In J. Pombo (Ed.), Proceedings of the Second International Conference on Railway Technology: Research, Development and Maintenance*. 2014.

Tables

Table 1 Details of parametric study for numerical tests

Simulation Set	Variables					Notes
	Numerical		Mechanical			
	Time step	Shearing speed	Damping	Contact stiffness	Inter-particle friction angle	
T1, 2, 3 & 4	Varied	0.2m/s	0.5	1GPa	30º	4 Tests @ 200kPa e=0.68
V4, 5 & 6	0.5	Varied	0.5	1GPa	40º	3 Tests @ 15kPa e=0.61
D7, 8, 9 & 10	0.5	0.2m/s	Varied	1GPa	35 º	4 Tests @ 15kPa e=0.61
CS11 &12	0.5	0.2m/s	0.5	Varied	30º	2 Tests @ 200kPa e=0.61, 0.62
IF13. 14 &15	0.5	0.2m/s	0.5	1GPa	Varied	3 Tests @ 15kPa e=0.61

Table 2 Particle size distribution of real and DEM ballast

% passing by weight (Network Rail Specification)	Sieve size (mm)	$^{1}/_{3}$ scale sieve size (mm)
100	62.5	20.83
85	50	16.67
17.5	40	13.33
12.5	31.5	10.5
1.5	22.4	7.47

Table 3. Differences in strength response for varying timestep. Confining pressure = 200 kPa, inter. friction = 30°, initial void ratio = 0.68 and contact stiffness = 1 GPa

Simulation no.	α_{sf}	Peak effective friction angle, degrees	Max. volumetric strain, %	Volumetric strain at end of simulation, %
TS1	0.25	42.18	1.287	-0.554
TS2	0.5	42.24	1.318	-0.504
TS3	0.95	42.68	1.365	-0.195
TS4	1.0	41.61	1.300	-0.181

Table 4. Variation in response induced by different strain rates. Confining pressure = 15 kPa, inter. friction = 40°, initial void ratio = 0.61 and contact stiffness = 1 GPa

Test no.	ε_q %/s	I_n	ϕ_{peak} (°)	Max. ϵ_{vol} (%)	Rate of dilation at ϕ_{peak}
V4	133	4.19×10^{-3}	52.44	0.136	0.833
V5	13.3	4.19×10^{-4}	49.67	0.145	0.717
V6	1.33	4.19×10^{-5}	49.01	0.153	0.655

Table 5 Variation in response caused by different damping constants. Confining pressure=15kPa, inter-particle friction=35°, initial void ratio = 0.61 and contact stiffness = 1 GPa

Test no.	α_d	approximate equivalent damping ratio, $\zeta \cong \frac{\alpha_d}{\pi}$	ϕ_{peak} (°)	Max. ϵ_{vol} (%)	Rate of dilation at ϕ_{peak}
D7	0.00	0.000	47.72	0.143	0.578
D8	0.05	0.016	47.86	0.145	0.595
D9	0.10	0.031	49.54	0.195	0.826
D10	0.70	0.223	54.21	0.189	0.714

Table 6. Variation in response caused by different contact stiffnesses. Confining pressure=200 kPa and inter-particle friction angle=30°

Test no.	e	Contact stiffness (GPa)	ϕ_{peak} (°)	Max. ϵ_{vol} (%)	Rate of dilation at ϕ_{peak}
CS11	0.67	1	41.61	1.30	0.132
CS12	0.68	10	42.21	0.71	0.667

Table 7 Variation in response induced by different ϕ_μ. Confining pressure = 15 kPa, initial void ratio = 0.61 and contact stiffness = 1 GPa

Test no.	ϕ_μ (°)	ϕ_{peak} (°)	Max. ϵ_{vol} (%)	Rate of dilation at ϕ_{peak}
IF13	30	46.69	0.30	0.387
IF14	35	48.03	0.17	0.554
IF15	40	49.77	0.14	0.730

Table 8 Calibration model parameters

Inter-particle friction angle ϕ_μ	40°
Contact stiffness K	1GPa
Particle Density ρ	2650kg/m^3
No. of particles	2780
Void ratio e	0.61
Shear velocity	0.02m/s
Damping constant α_d	0.05
Timestep safety factor α_{sf}	0.5
Specimen dimensions	294mm×150mm

Figures

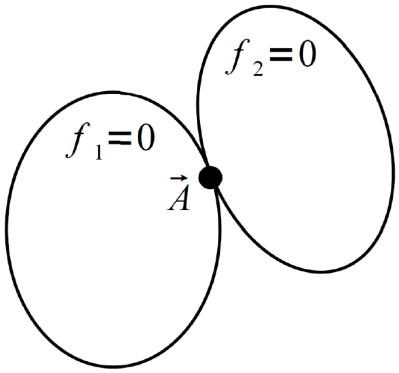

Figure 1. Two elliptical potential particles in contact at point *A*.

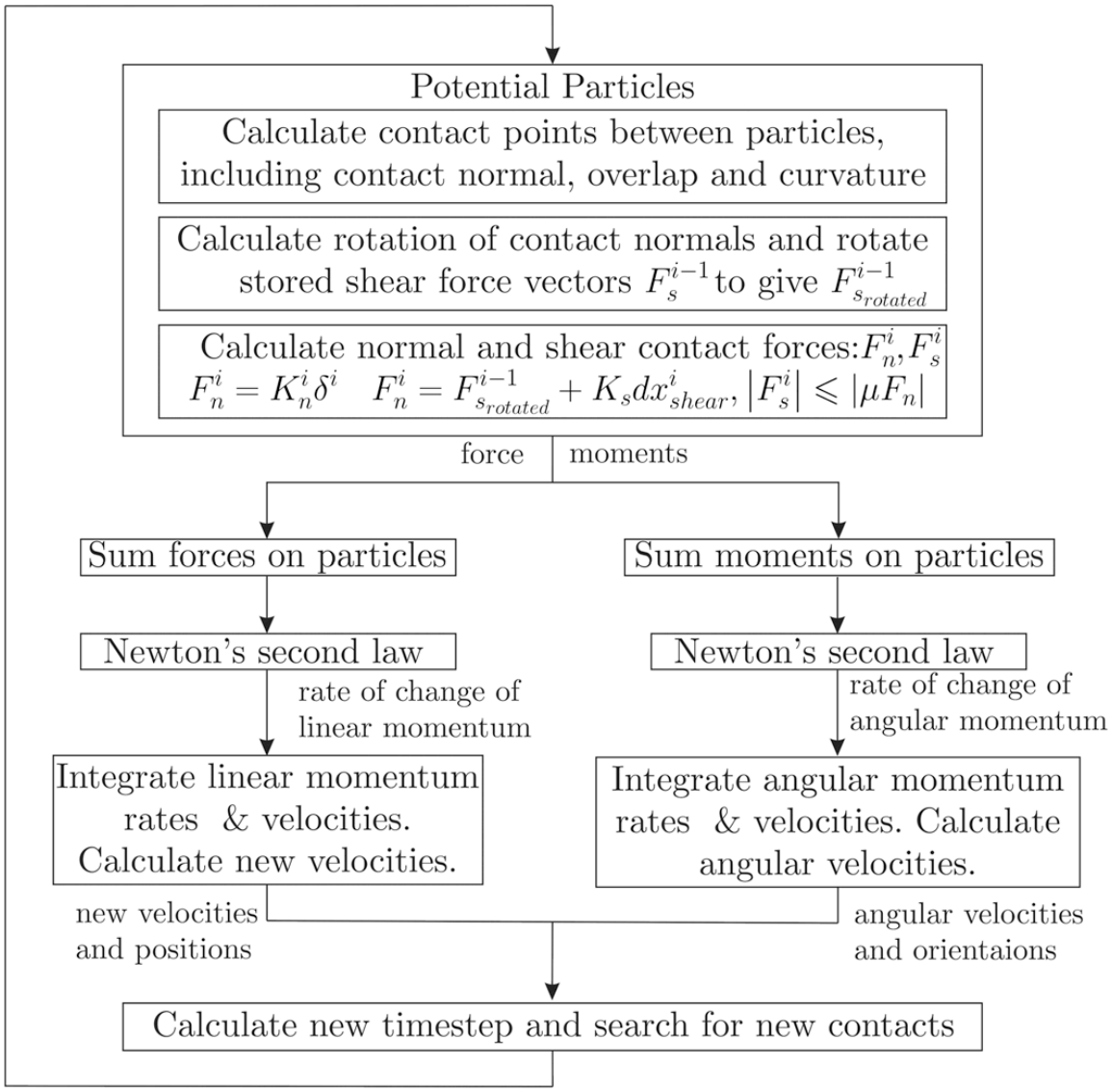

Figure 2. DEM simulation cycle [7]

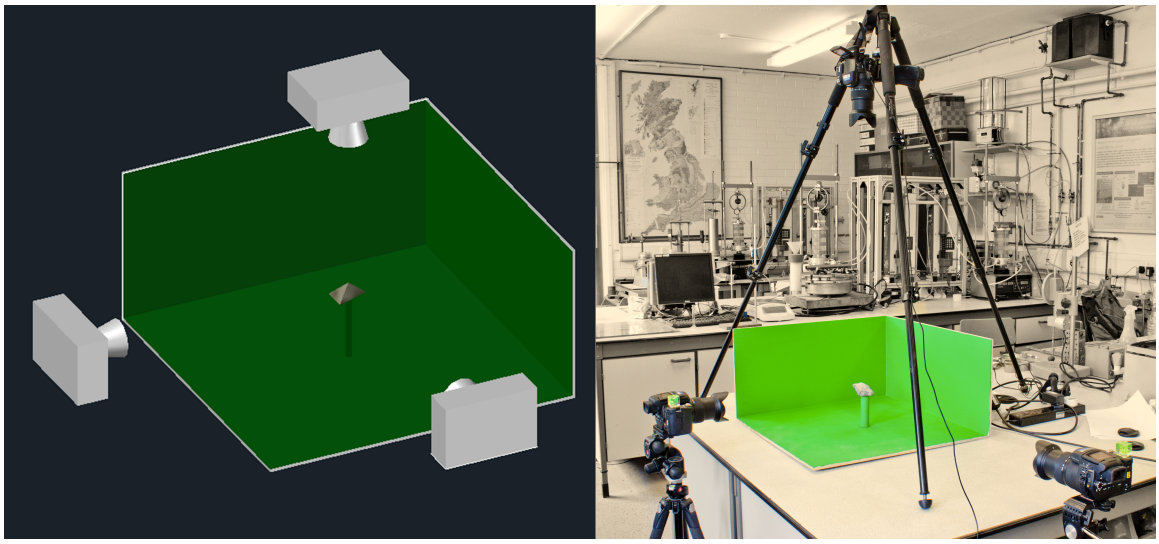

Figure 3. Experimental setup for particle characterization. Three cameras are used to capture 3 orthogonal views of a particle. A green background is used to make segmentation robust.

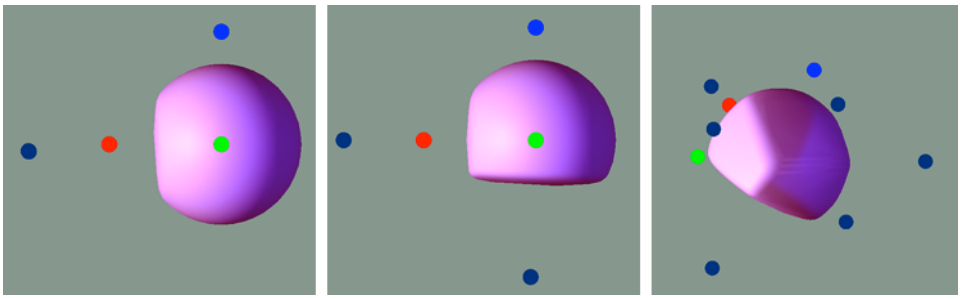

Figure 4. The creation of a DEM ballast particle. From left to right more flats are added to the initial sphere until the desired shape has been achieved. The smaller dots are control nodes used to manipulate the flat positions

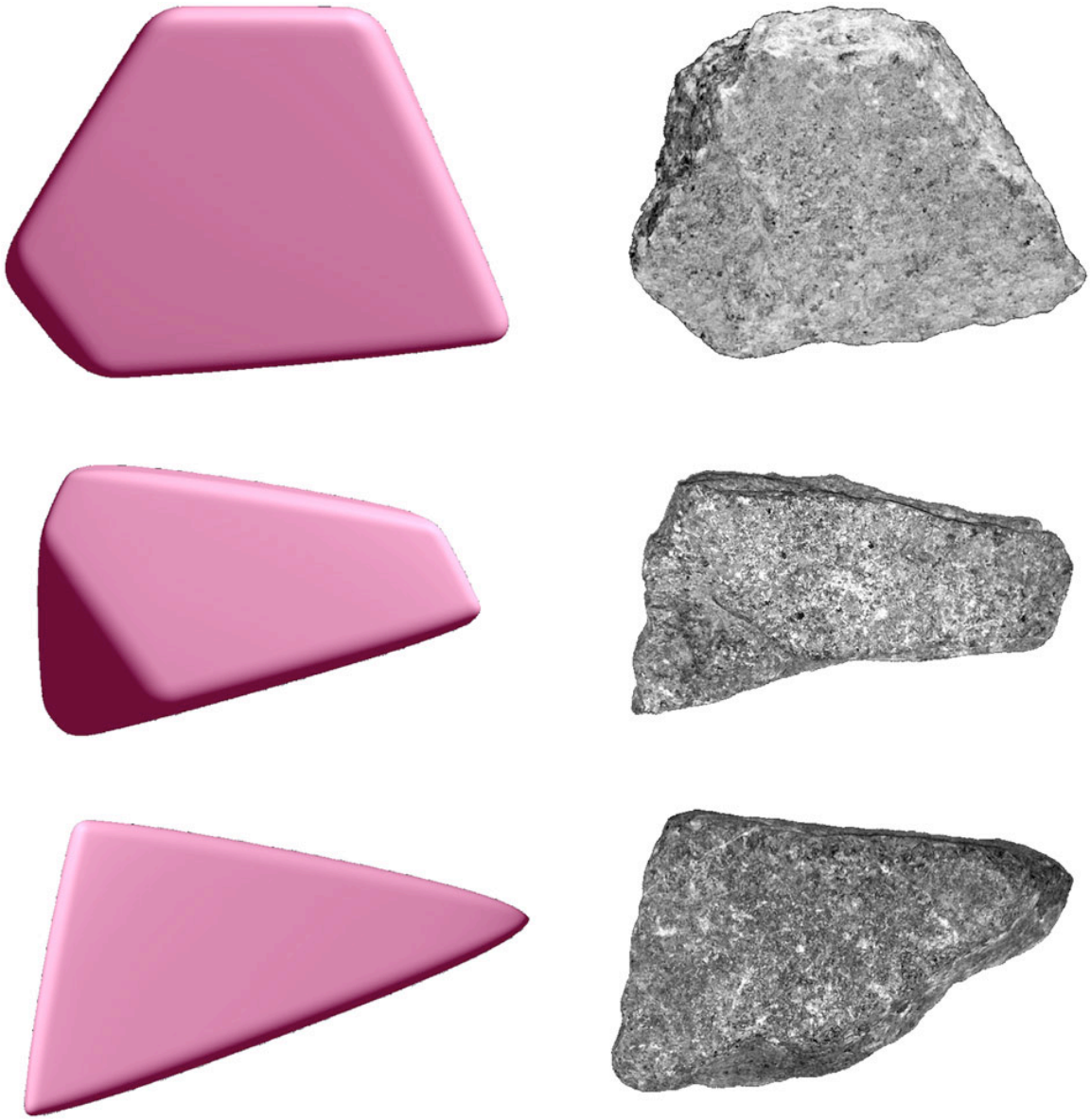

Figure 5. Example numerical ballast particle with its real counterpart

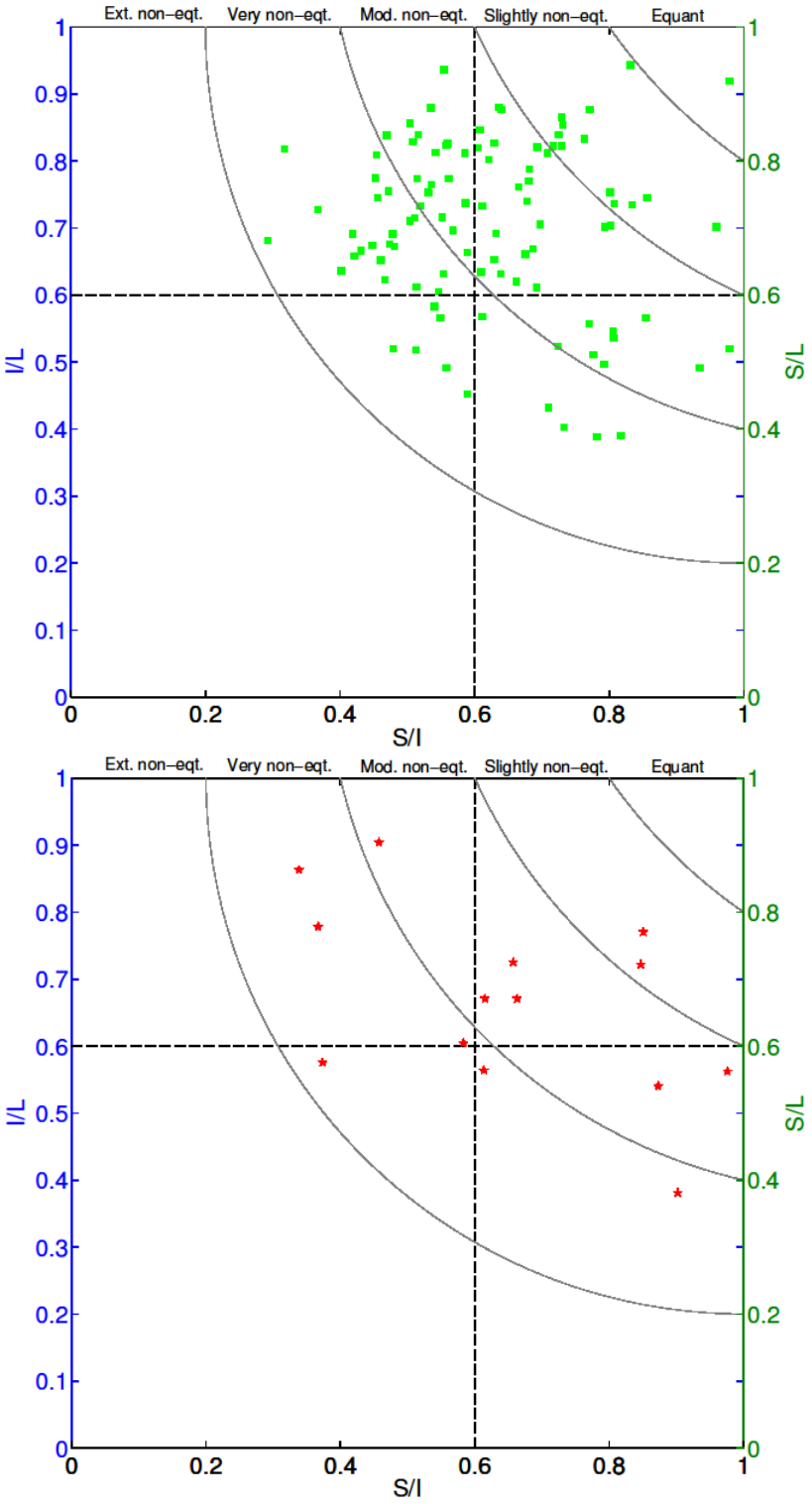

Figure 6: Zingg plots of I/L against S/I for (a) real ballast and (b) DEM ballast

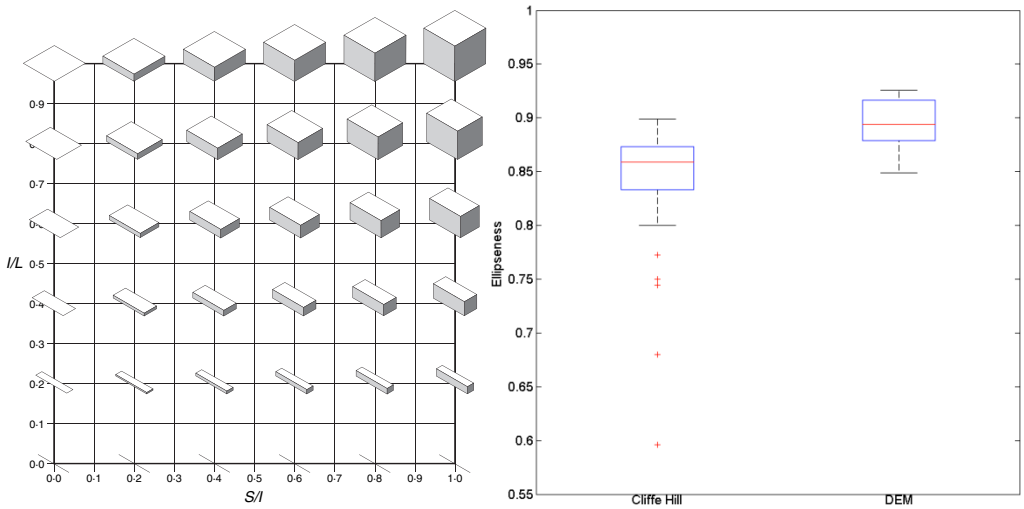

(a) (b)

Figure 7 (a) Visual key for Zingg plot (b) Ellipseness ratio for real and DEM ballast

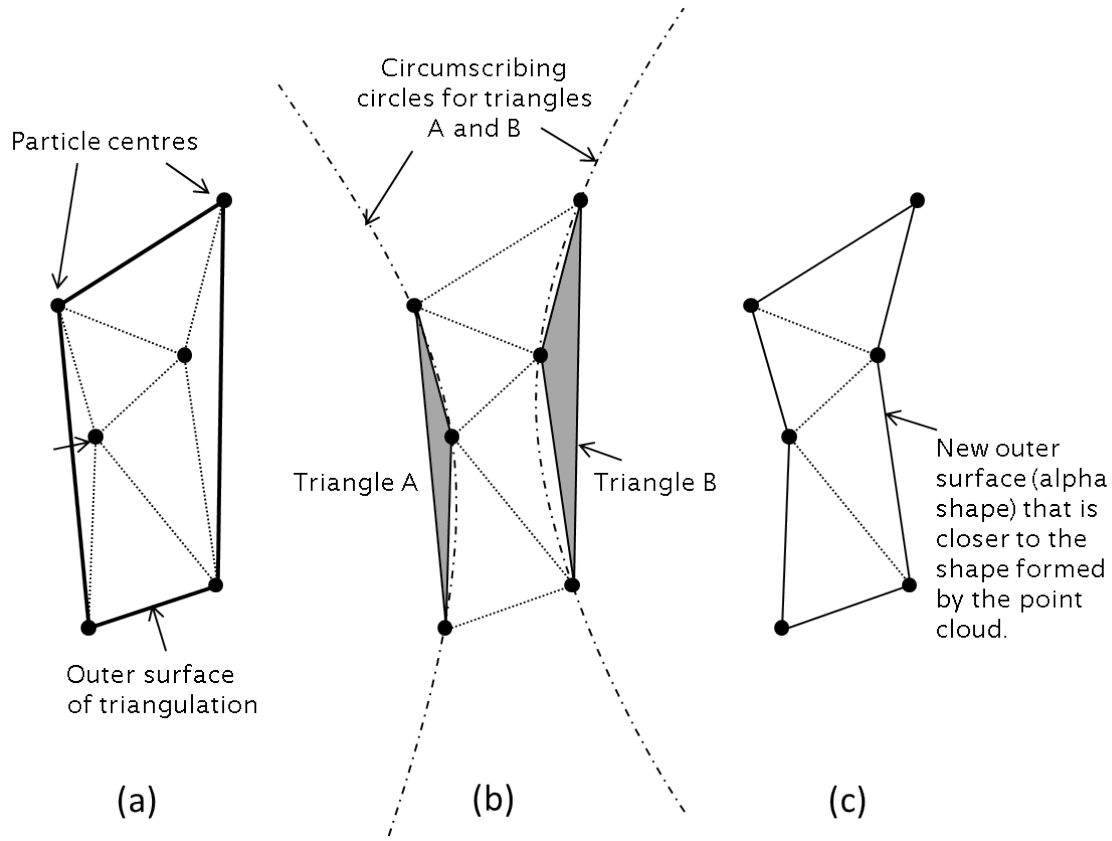

Figure 8. Example of alpha shape formation for 2-dimensional point cloud

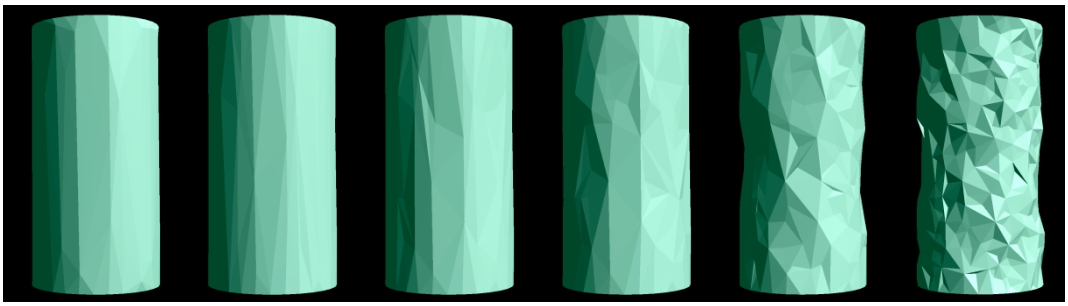

Figure 9. Sequence of alpha shapes with parameter α reducing from left $(\alpha = \infty)$ to right $\alpha = (maximum\ particle\ radius * 1.5)^2$

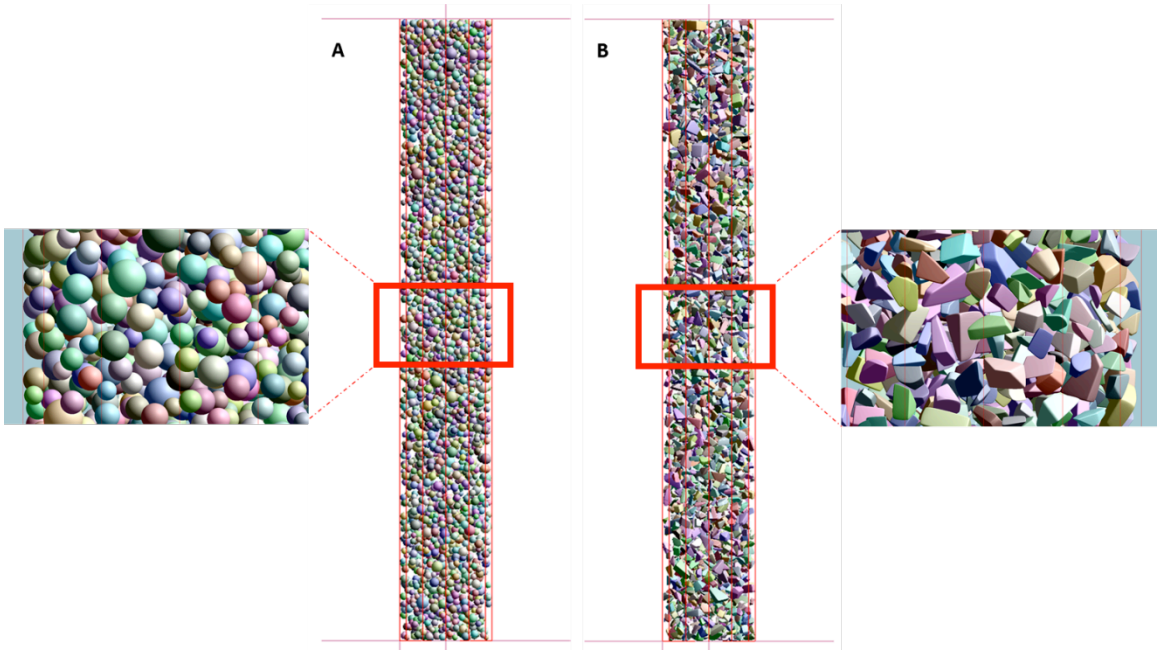

Figure 10. Specimen preparation. a) spheres are randomly distributed in a cylinder b) spheres are replaced by potential particles(DEM ballast)

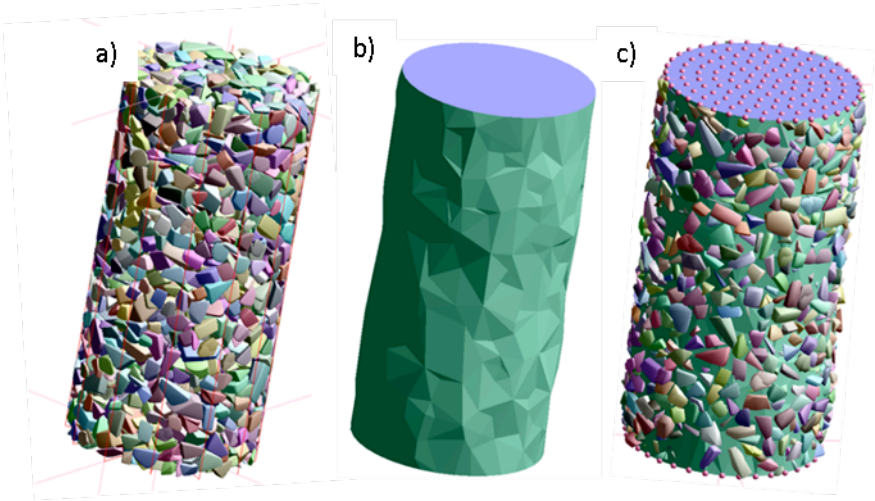

Figure 11. Numerical triaxial specimens. a) Particles in a typical specimen b) the virtual membrane and c) specimen showing virtual particles on the top/bottom platen

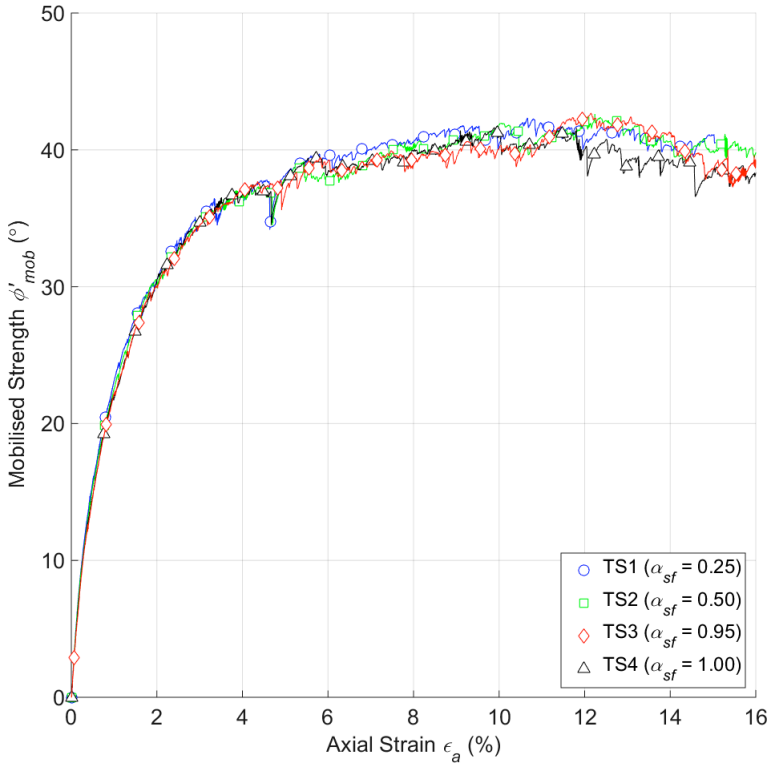

(a)

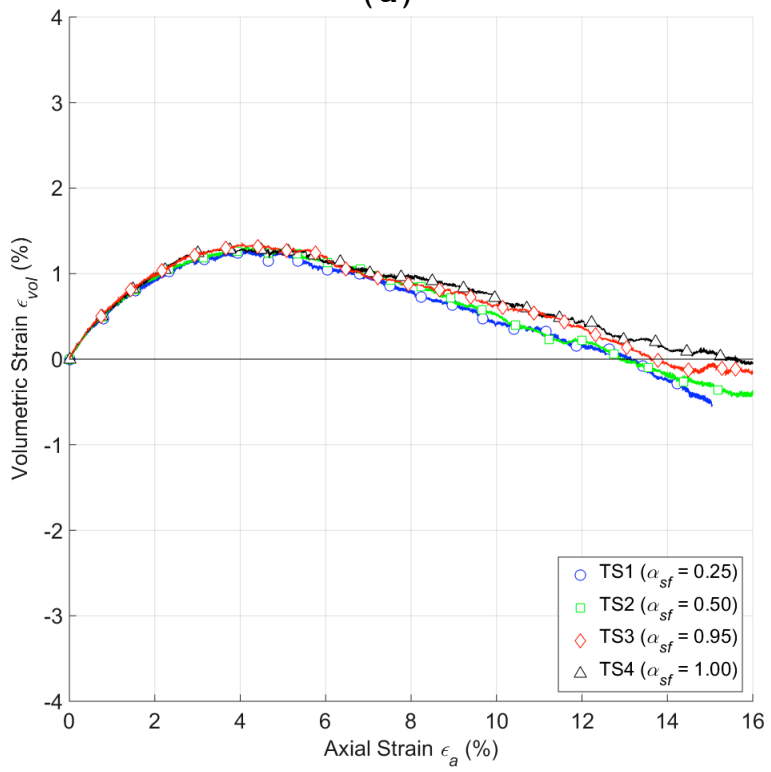

(b)

Figure 12 Effects of different timesteps on (a) Mobilized friction angle and (b) volumetric strain versus axial strain

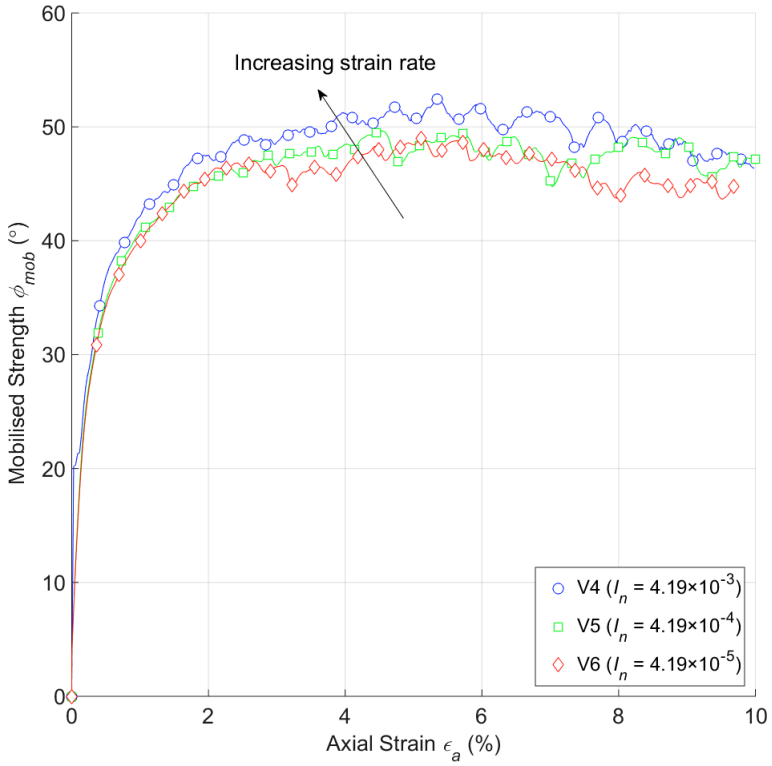

(a)

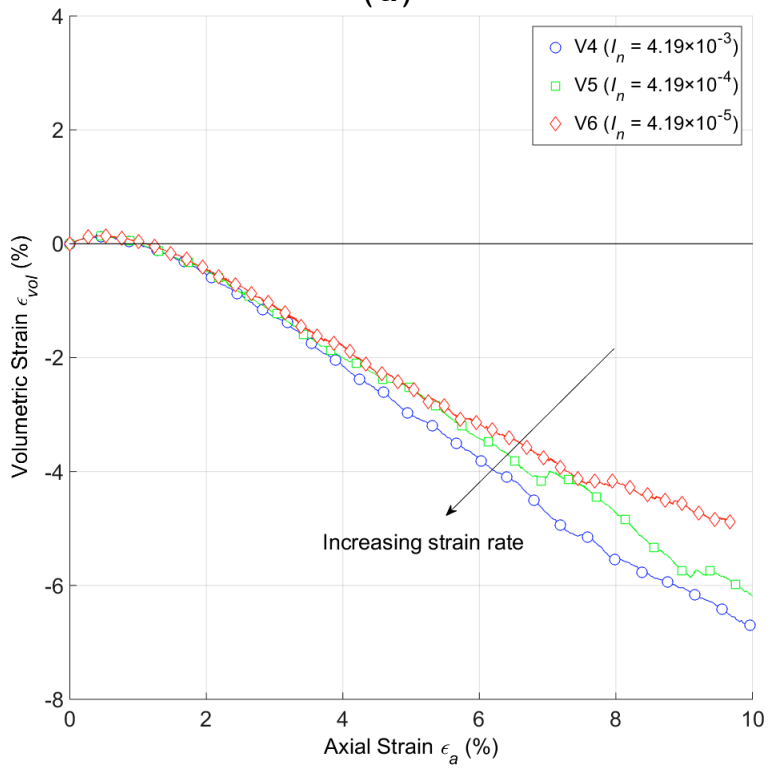

(b)

Figure 13 Effects of different shear rates on (a) Mobilized friction angle and (b) volumetric strain versus axial strain.

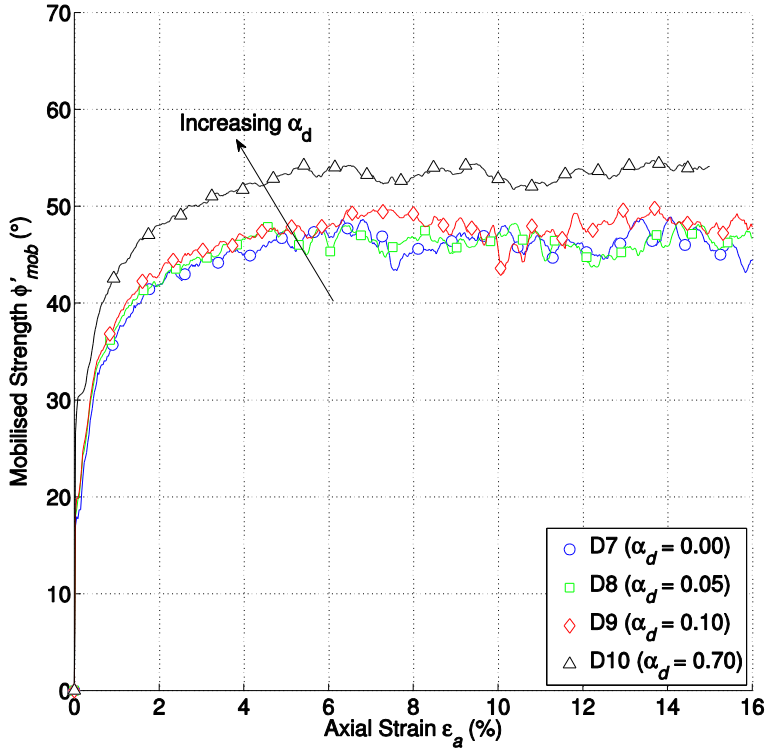

(a)

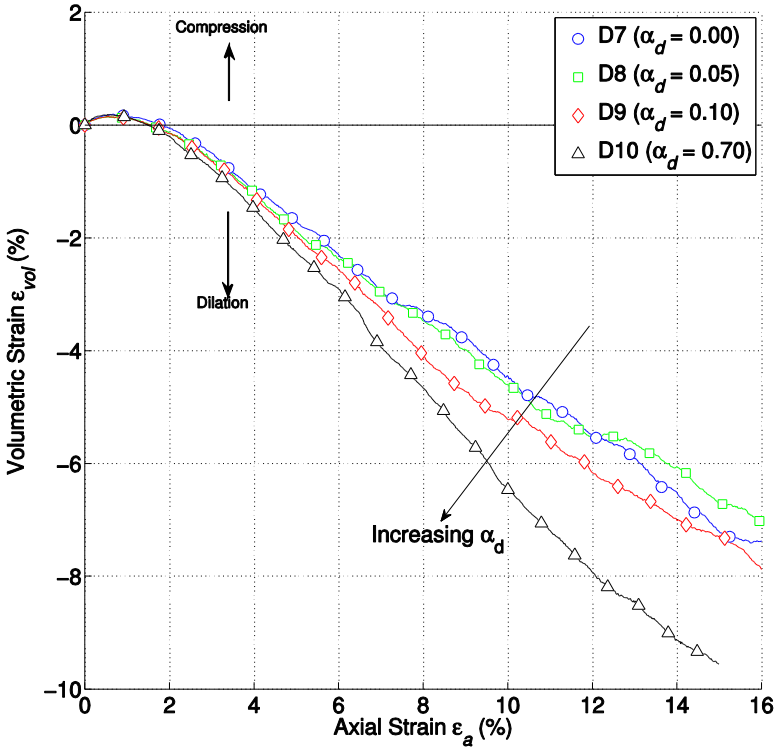

(b)

Figure 14 Effects of damping on (a) mobilized shear strength and (b) volumetric strain versus axial strain

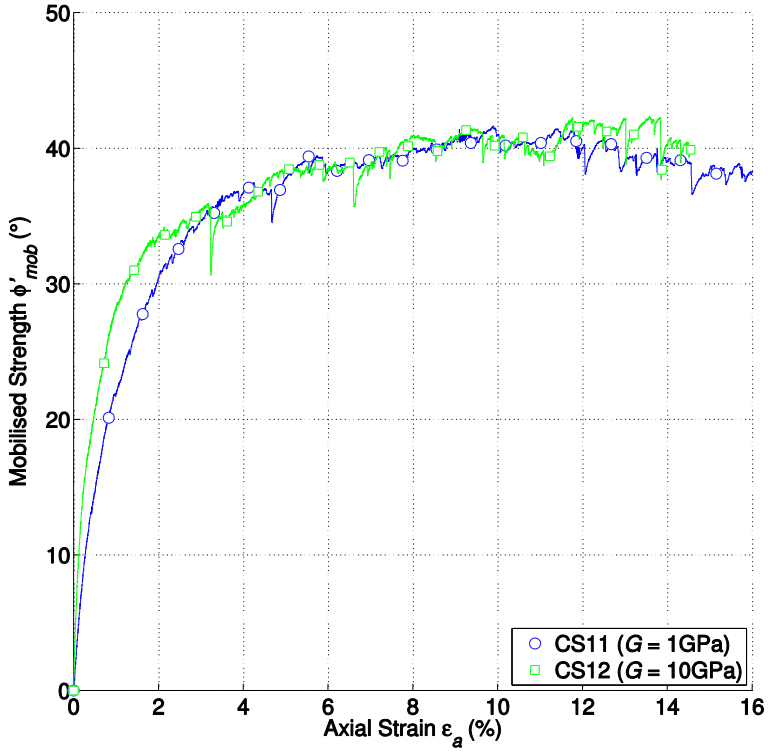

(a)

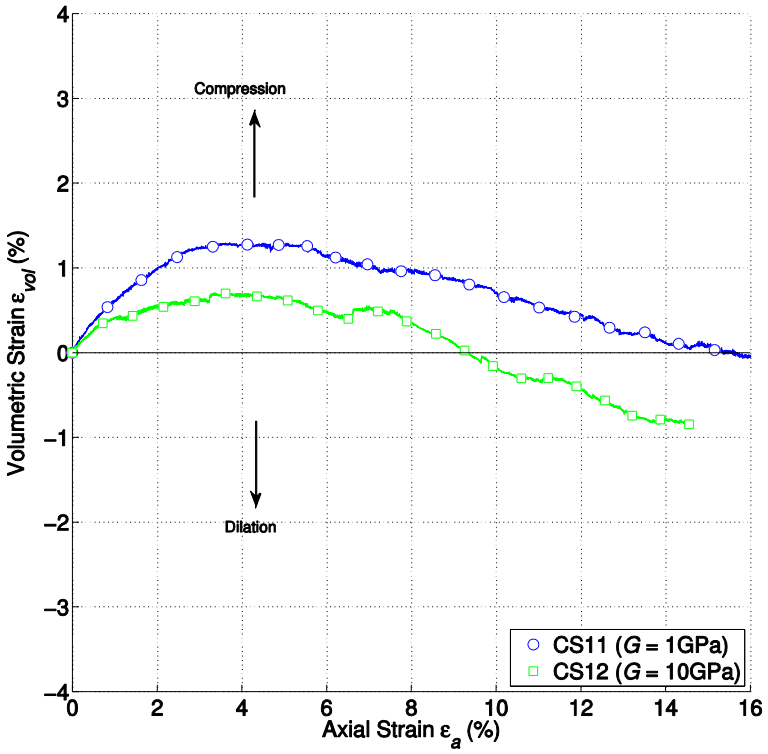

(b)

Figure 15 Effect of contact stiffness variation on (a) Mobilized shear strength and (b) Volumetric strain versus axial strain

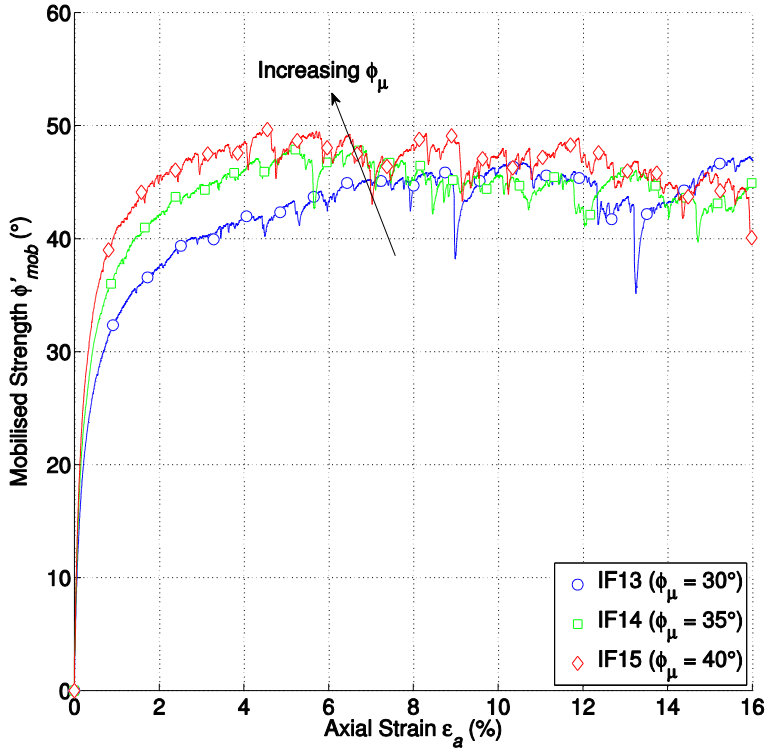

(a)

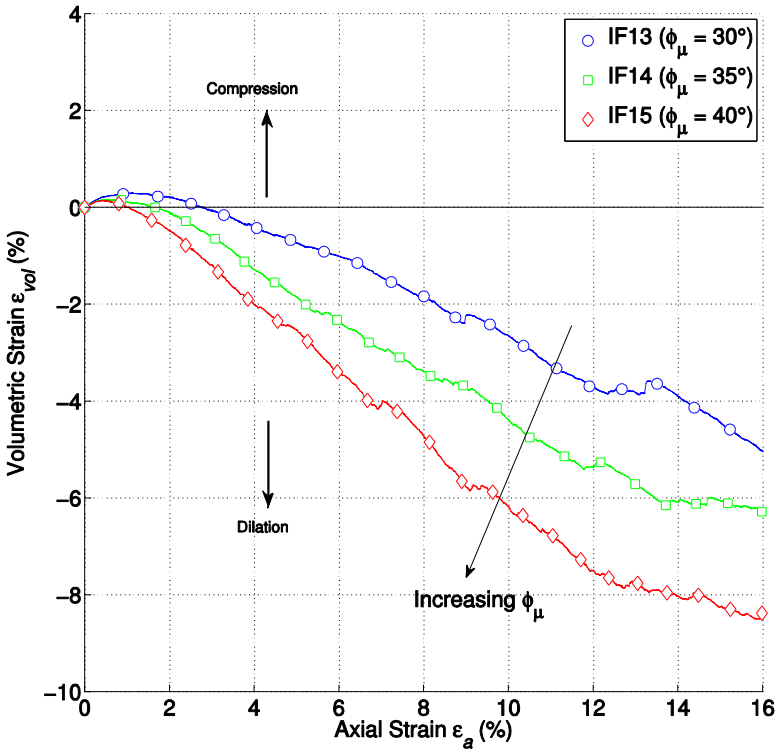

(b)

Figure 16 The effects of variation in inter-particle friction on (a) Mobilized shear strength and (b) Volumetric strain versus axial strain

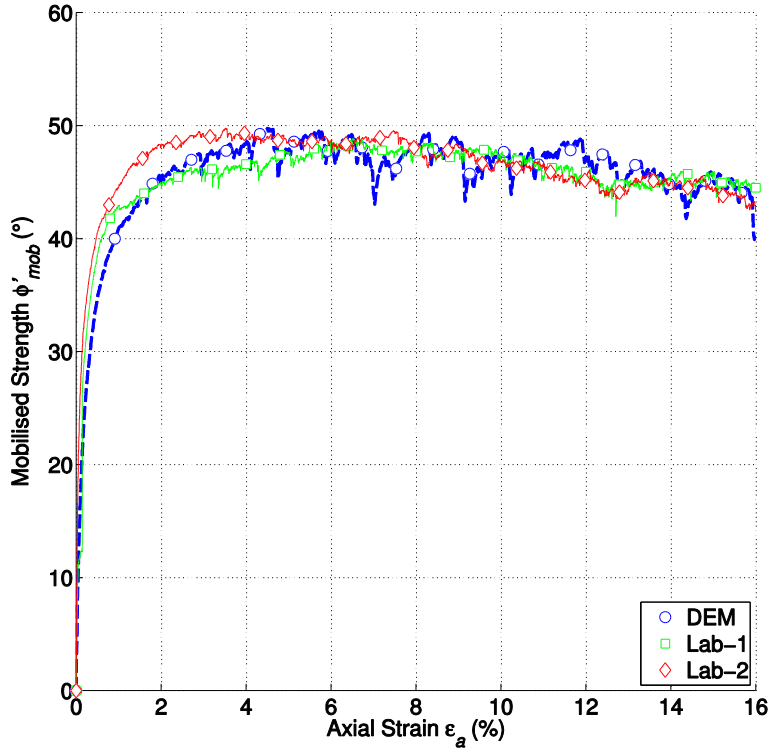

(a)

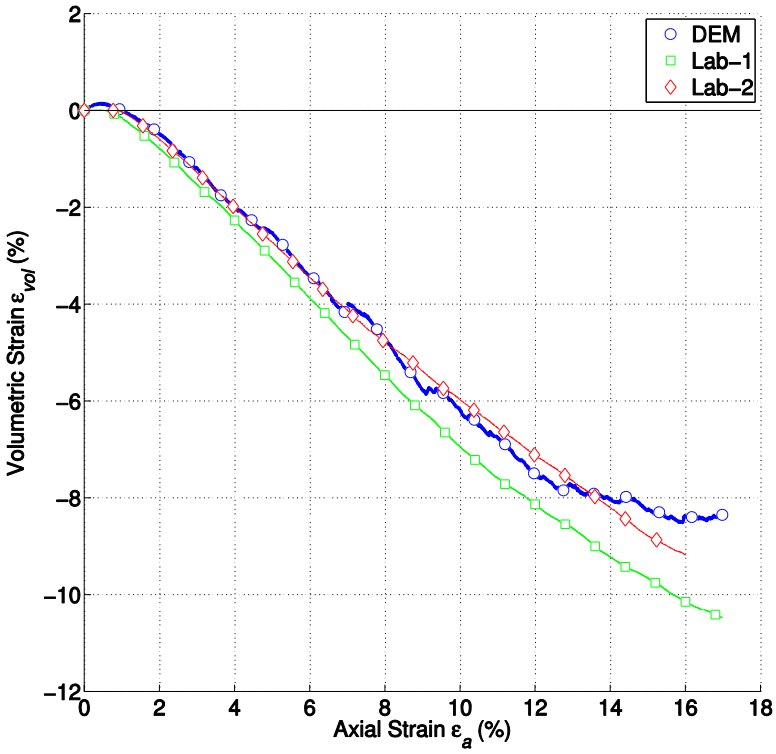

(b)

Figure 17 Comparison of DEM and two laboratory experiments (at 15kPa) results